

1
2
3
4
5
6
7
8
9
10
11
12
13
14
15
16
17

**Application of a new scheme of cloud base droplet nucleation in a
Spectral (bin) Microphysics cloud model: sensitivity to aerosol size
distribution**

E. Ilotoviz and A. Khain

Department of Atmospheric Sciences, The Hebrew University of Jerusalem, Israel

Submitted to Atmos. Chem. Phys. Discuss.

June 2016

Revised

21 September 2016

Communicating author: Alexander Khain, Department of Atmospheric Sciences, The Hebrew
University of Jerusalem, Israel, email: alexander.khain@mail.huji.ac.il

18 **Abstract**

19 A new scheme of droplet nucleation at cloud base is implemented into the Hebrew University
20 Cloud Model (HUCM) with spectral (bin) microphysics. In this scheme, supersaturation
21 maximum S_{max} near cloud base is calculated using theoretical results according to which
22 $S_{max} \sim w^{3/4} N_d^{-1/2}$, where w is the vertical velocity at cloud base and N_d is droplet concentration.
23 Microphysical cloud structure obtained in the simulations of a mid-latitude hail storm using the
24 new scheme is compared with that obtained in the standard approach, in which droplet nucleation
25 is calculated using supersaturation calculated in grid points. The simulations were performed
26 with different concentrations of cloud condensational nuclei (CCN) and with different shapes of
27 CCN size spectra. It is shown that the new nucleation scheme substantially improves the vertical
28 profile of droplet concentration shifting the concentration maximum to cloud base. It is shown
29 that the effect of the CCN size distribution shape on cloud microphysics is not less important
30 than the effect of the total CCN concentration. It is shown that the smallest CCN with diameters
31 less than about $0.015 \mu m$ have a substantial effect on mixed-phase and ice microphysics of deep
32 convective clouds. Such CCN are not measured by standard CCN probes which hinders
33 understanding of cold microphysical processes.

34

35 Key words: cloud-aerosol interaction, droplet nucleation at cloud base, spectral bin
36 microphysics

37

38

39

40

41 1. Introduction

42 Droplet concentration is the key microphysical parameter that affects precipitation formation,
43 and radiative cloud properties (Pruppacher and Klett, 1997). The droplet concentration determines
44 major microphysical cloud properties such as height of precipitation onset, type of precipitation
45 (liquid, mixed phase and ice) (Khain, 2009; Freud and Rosenfeld, 2012; Tao et al. 2012) . Droplet
46 concentration is determined by concentration and size distribution of aerosol particles (AP) and by
47 the maximum value of supersaturation near cloud base S_{\max} . S_{\max} is reached at a few tens of
48 meters above cloud base (Rogers and Yau, 1996). The vertical grid spacing of most cloud-
49 resolving models is too coarse to resolve this maximum. This can lead to errors in determination
50 of droplet concentration. Therefore, it is desirable to parameterize the process of droplet
51 nucleation near cloud base. One approach to the parameterization is based on lookup tables
52 developed using precise 1D parcel models (e.g., Segal and Khain, 2006). The other approach is
53 based on analytical calculation of supersaturation maximum, S_{\max} , near cloud base. This approach
54 has been developed in several studies using various assumptions concerning CCN activity spectra
55 (Ghan et al., 1993, 1997; Bedos et al., 1996; Abdul-Razzak et al., 1998; Cohard et al., 1998;
56 Abdul-Razzak and Ghan, 2000; Fountoukis, 2005; Shipway and Abel, 2010). In these studies
57 calculation of a supersaturation maximum is reduced to solving a complicated integro-differential
58 equation assuming different expressions for CCN activation spectra. The parameters of activation
59 CCN spectra, as well as the concentration and shape of the CCN size distributions, are often
60 prescribed in atmospheric models and assumed to be invariant over time. The results and a
61 comparison of these approaches are presented by Ghan et al. (2011).

62 In cloud models with a comparatively high resolution (Kogan 2001; Khain et al. 2014)
63 supersaturation S_w is calculated explicitly at each grid point. In these bin microphysics models AP
64 playing the role of cloud condensational nuclei (CCN) are described using aerosol size distribution
65 functions containing several tens of size bins. The value of supersaturation is used to calculate the
66 critical radius of AP using the Köhler theory. All CCN with sizes exceeding this critical value are
67 activated to droplets. This approach will be referred to as standard approach (ST) where
68 supersaturation maximum near cloud base is not resolved and the vertical profile of
69 supersaturation may not contain such maximum. It leads to underestimation of droplet
70 concentration in clouds, at least in their low part.

71 In set of studies by Pinsky et al. (2012, 2013, 2014) formation of profiles of supersaturation
72 and of droplet concentration were investigated both analytically and by means of a high precision
73 model of an ascending adiabatic parcel. Pinsky et al. (2012) proposed a simple method of
74 calculating S_{\max} near cloud base for monodisperse aerosol size distribution. The detailed test
75 showed that the method can be applied to any CCN spectra. Pinsky et al (2014) gave a theoretical
76 basis for such conclusion by calculating droplet concentrations using multidisperse size spectra of
77 AP. The method of calculating droplet concentration near cloud base using S_{\max} will be referred to
78 as *new approach* (NA).

79 In this study we investigate the effects of application of NA on the microphysics of mid-
80 latitude deep convective clouds (hail storm) using the Hebrew University Cloud model (HUCM)
81 with spectral-bin microphysics (SBM). The effect of the new approach is investigated in
82 simulations with different parameters of CCN activation spectra.

83

84 **2. Model description**

85 The HUCM is a 2-D, nonhydrostatic SBM model with microphysics based on solving a
86 system of equations for size distributions of liquid drops, three types of pristine ice crystals
87 (plates, columns, and dendrites), snow/aggregates, graupel, hail and partially frozen or "freezing
88 drops". Each size distribution is discretized into 43 mass-doubling bins, with the smallest bin
89 equivalent to the mass of a liquid droplet of radius $2 \mu m$. AP playing the role of CCN are also
90 defined on a mass grid containing 43 mass bins. The size of dry CCNs ranges from $0.005 \mu m$ to 2
91 μm .

92 Primary nucleation of each ice crystal type is described using Meyers et al. [1992]
93 parameterization. The type of ice crystals is determined depending on temperature range where
94 the particles arise (Takahashi et al., 1991). Secondary ice generation is taken into account during
95 riming (Hallett and Mossop 1974). Collisions are described by solving the stochastic collection
96 equations for the corresponding size distributions using the Bott (1998) method. Height-
97 dependent, gravitational collision kernels for drop-drop and drop-graupel interactions are taken
98 from Pinsky et al. (2001) and Khain et al. (2001); those for collisions between ice crystals are
99 taken from Khain and Sednev (1995) and Khain et al. (2004). The latter studies include the
100 dependence of particle mass on the ice crystal cross-section. The effects of turbulence on
101 collisions between cloud drops are included (Benmoshe et al. 2012). The collision kernels depend
102 on the turbulence intensity and changes over time and space.

103 The time-dependent melting of snow, graupel, and hail as well as shedding of water from hail
104 follows the approach suggested by Phillips et al. (2007). We have implemented liquid water mass
105 in these hydrometeor particles that is advected and settle similarly to the mass of the
106 corresponding particles. As a result, these particles are characterized by their total mass and by the
107 mass of liquid water (i.e., the liquid water mass fraction). The liquid water fraction increases

108 during melting. As soon as it exceeds ~95%, the melting particles are converted to raindrops.
109 Process of time dependent freezing is described according to Phillips et al. (2014, 2015). The
110 freezing process consists of two stages. The first nucleation stage is described using the
111 parameterization of immersion drop freezing proposed by Vali (1994) and Bigg (1953). Drops
112 with radii below $80 \mu m$ that freeze are assigned to plates, whereas larger drops undergoing
113 freezing are assigned to freezing drops. The freezing drops consist of a core of liquid water
114 surrounded by an ice envelope. Time-dependent freezing of liquid within freezing drops is
115 calculated by solving the heat balance equations that take into account the effects of accretion of
116 supercooled drops and ice particles. Collision between freezing drops and other hydrometeors lead
117 either to the freezing drops category if the freezing drop is larger than its counterpart. Otherwise,
118 the resulting particle is assigned to the type of counterpart. Once the liquid water fraction in a
119 freezing drop becomes less than some minimal value (<1%) it is converted to a hailstone. Hail can
120 grow either by dry growth or by wet growth (Phillips et al. 2014, 2015). Accordingly, liquid water
121 is allowed in hail and graupel particles at both positive and negative temperatures. The shedding
122 of water in wet growth is also included.

123 Water accreted onto aggregates (snow) freezes immediately at temperatures below $0^{\circ}C$,
124 where it then contributes to the rimed fraction. This rimed mass distribution is advected and settle
125 similarly to the snow masses. Riming mass increases the density of the aggregates. As the bulk
126 density of snow in a certain mass bin exceeds a critical value ($0.2 g cm^{-3}$), the snow from this bin
127 is converted into graupel. The appearance of water on the surface of hailstones as well as an
128 increase in the rimed fraction of snowflakes affect the particle fall velocities and coalescence
129 efficiencies.

130 The initial size distribution of CCN (at $t=0$) is calculated using the empirical dependence (i.e.,
131 the Twomey formula) of concentration N_{ccn} of activated CCN on supersaturation S_w (in %)
132 $N_{ccn} = N_o S_w^k$, where N_o and k are the measured constants (Khain et al., 2000). The obtained
133 aerosol size distribution is corrected in zones of very small and very large CCN, that is, in size
134 ranges where the Twomey formula is invalid. At $t>0$ the prognostic equation for the size
135 distribution of non-activated CCN is solved. Using the value of S calculated at each time-step and
136 in each grid point, the critical radius of CCN particles was determined according to the Köhler
137 theory. The CCNs with radii exceeding the critical value are activated and new droplets are
138 nucleated. The corresponding bins of the CCN size distributions become empty. In ST, this
139 procedure is used at all cloud grid points.

140 In NA, droplet concentration at cloud base is calculated using the formula for S_{max} derived
141 by
142 Pinsky et al. (2012)

$$143 \quad S_{max} = C w^{3/4} N_d^{-1/2}, \quad (1)$$

144 where w is vertical velocity at cloud base, N_d is droplet concentration and coefficient C slightly
145 depends on the thermodynamical parameters only (see **Table 1** for notations). A brief derivation
146 of the formula (1) is presented in **Appendix**. Since the droplet concentration at cloud base is equal
147 to the concentration of CCN activated at $S_w = S_{max}$, the droplet concentration at the cloud base can
148 be calculated as:

$$149 \quad N_d = \int_{r_{n-cr}(S_{max})}^{\infty} f(r_n) dr_n \quad (2)$$

150 where $f(r_n)$ is a size distribution of dry AP and r_{n_cr} is critical radius of CCN activated under

151 S_{\max} . According to the Köhler theory, the critical radius relates to S_{\max} as

$$152 \quad r_{n_cr} = \frac{A}{3} \left(\frac{4}{BS_{\max}^2} \right)^{1/3}, \quad (3)$$

153 where coefficients A and B are the coefficients of the Köhler equation for equilibrium

154 supersaturation (see Table 1 for notations). Substituting Eq. (2) into (1) one can obtain equation

155 for S_{\max} :

$$156 \quad S_{\max} \left[\underbrace{\int_{r_{n_cr}(S_{\max})}^{\infty} f(r_n) dr_n}_{N_d} \right]^{1/2} = Cw^{3/4} \quad (4)$$

157 Taking into account the relationship (3), Eq. (4) contains only one unknown S_{\max} . This

158 equation is easily solved by iteration calculating S_{\max} , $r_{n_cr}(S_{\max})$ and concentration of nucleated

159 droplets at cloud base at each time step.

160 The values of S_{\max} were calculated ~~in~~ at all grid points corresponding to cloud base, which is

161 determined as the first grid point from below, ~~in~~ at which $S_w \geq 0$.

162

163 3. Design of simulations

164 All simulations were performed within a computational domain of 153.9 km x 19.2 km, and

165 a grid spacing of 300 m in the horizontal direction and 100 m in the vertical direction. Effects of

166 NA on cloud microphysics were tested in simulations of a thunderstorm observed in Villingen-

167 Schwenningen, southwest Germany, on June 28, 2006. Meteorological conditions (including

168 sounding) of this storm are described by Khain et al. [2011]. The background wind direction was

169 quasi-2-D, which simplified the prescription of the background wind profile in the 2-D model. The
170 wind speed increased with height from $\sim 10 \text{ m s}^{-1}$ in the lower atmosphere to about 20 m s^{-1} at
171 levels of 100-200 mb. Surface temperature was 22.9°C , the relative humidity near the ground was
172 high ($\sim 85\%$), which led to a low lifting condensation level of about 890 m. The freezing level was
173 located at around 3.5 km. The observed maximum diameter of hailstones was about 5 cm.

174 The convection was triggered by a cool pool, which is typical in simulations of long-lasting
175 convection (Rotunno and Klemp, 1985).

176 Three sets of simulations were performed, each simulation in two versions: according to ST
177 where the critical CCN radius was calculated using a supersaturation calculated at the grid points
178 using the values of temperature and humidity, and according to NA where the critical CCN radius
179 and S_{max} were determined from Eq. (9).

180 *The first set of simulations* aims at the comparison of the microphysics between NA and ST
181 in cases of high ($N_0 = 3500 \text{ cm}^{-3}$) and low ($N_0 = 100 \text{ cm}^{-3}$) CCN concentrations. Minimum
182 CCN radii were set equal to $0.015 \text{ }\mu\text{m}$ and $0.0125 \text{ }\mu\text{m}$, respectively. These values correspond to
183 the data according to which **the nuclei mode (the smallest CCN) in Marine aerosol size**
184 **distribution contains aerosols smaller than the nuclei mode in Continental case or even than in**
185 **Urban case** (Ghan et al, 2011). Similar CCN size distributions were used by Khain et al (2011).
186 These simulations are referred to as E3500, E100 (T) and EN3500, EN100 (NA), respectively.

187 *In the second set of simulations* the smallest CCN were added into the AP spectra. The large
188 impact of the smallest CCN in formation of ice crystals in cloud anvils was shown by Khain et al.
189 (2012). The minimum CCN radii were taken equal to $0.006 \text{ }\mu\text{m}$ and $0.003 \text{ }\mu\text{m}$ in cases of high
190 and low CCN concentrations, respectively. These simulations are referred to as E3500-S, EN3500-
191 S, E100-S and EN100-S, where symbol "S" denotes small AP.

192 In the first and the second sets of simulations the slope parameter k was assumed equal to 0.9.
193 *The third set of simulations* was similar to the second one, but with the slope parameter k
194 =0.5. In many studies investigating effects of aerosols on cloud microphysics only parameter N_0
195 is changed. However, the slope parameter determines the relationship between concentration of
196 smaller and larger CCN, so concentration of nucleated droplets also depends on the slope
197 parameter. The simulations of the third set are referred to as E3500-S-05, EN3500-S-05, E100-S-
198 05 and EN100-S-05. Size distributions of CCN in the simulations are shown in **Figure 1**.

199 CCN concentrations in the simulations are presented in **Table 2**. Although the difference
200 between the total aerosol concentrations is not large, in case $k=0.5$ the CCN size distribution
201 contains more large CCN and fewer small CCN. These size distributions were assumed within the
202 lower 2-km layer. Above this level, the CCN concentration in each mass bin was decreased
203 exponentially with height. **Above 8 km, the CCN concentration was set constant.**

204

205 4. Results of simulations

206

207 4.1 Vertical profiles of supersaturation near cloud base

208 The model calculates supersaturation at the model grid points which typically do not
209 exactly coincide with the cloud base level where supersaturation $S_w=0$. We consider the first level
210 where $S_w \geq 0$ as the cloud base. Since the supersaturation maximum is reached not far from the
211 cloud base level, especially for high AP concentration cases (Pinsky et al. 2012), we attribute the
212 values of S_{\max} to this level. Correspondingly, the difference between NA and ST in the droplet
213 concentrations is also attributed to this level. **Figure 2** shows vertical profiles of supersaturation
214 calculated in ST and NA simulations in the atmospheric columns where the velocity at cloud base

215 was equal to 1 ms^{-1} . It is natural that the values of S_{max} are larger in case of low CCN
216 concentration as compared to high CCN concentration case. For goals of the present study, a more
217 interesting finding is that the values of S_{max} calculated using NA are substantially larger than S_w
218 calculated at model level associated to the cloud base in ST. The difference between NA and ST in
219 the supersaturation values leads to a substantial difference in the droplet concentrations, especially
220 in cases of high CCN concentration. Calculation of S_{max} at cloud base changes the vertical profile
221 of supersaturation above it. While in ST supersaturation changes only slightly or even increase
222 with height within 100-200 m above cloud base, in NA supersaturation decreases within this layer
223 above the supersaturation maximum in agreement with the theory (Rogers and Yau, 1989, Pinsky
224 et al, 2012, 2013).

225 To justify the values of supersaturation and droplet concentration obtained in NA,
226 benchmark simulations using a parcel model were performed. The parcel model describes AP and
227 drops using drop size distribution defined on a mass grid containing 2000 mass bins (Pinsky et al,
228 2002). It calculates growth of AP and droplets by solving the equation for diffusional growth
229 written in the most general form without using parameterization of droplet nucleation. Time step
230 used for solving the diffusional growth equation was 0.001 s. The model was used earlier for
231 developing lookup tables relating parameters of AP and vertical velocity to droplet concentration
232 (Segal and Khain, 2006). Simulations with the parcel model were performed for the same vertical
233 velocity at cloud base, temperature and CCN distributions as in the HUCM simulations. As can be
234 seen from Fig. 2, the values of supersaturation and droplet concentration calculated using NA are
235 much closer to those calculated using the parcel model as compared to the values calculated using
236 ST.

237 The model level associated with the cloud base (where $S_w \geq 0$) is slightly higher than the
238 lifting condensation level (LCL), where $S_w = 0$. At the same time, the calculations performed
239 according to Pinsky et al. (2012) show that the level where $S_w = S_{\max}$ is located from about 20 m
240 (for high CCN concentration) to about 60 m (for low CCM concentration) higher than the LCL.
241 The estimations show, therefore, that the level where $S_w = S_{\max}$ is quite close to the model cloud
242 base level. Accordingly, the droplet concentration determined at $S_w = S_{\max}$ is assigned to the
243 corresponding grid point at the model cloud base.

244

245 *4.2 High CCN concentration*

246 In this section we compare the results for three pairs of simulations of clouds were
247 developing in a highly polluted atmosphere. **Figure 3** shows the fields of droplet concentration N_d
248 at the developing stage of the cloud evolution in E3500-S-0.5 (a), EN3500-S-0.5 (b), E3500-S (c)
249 and EN3500-S (d). The maximum N_d in NA is reached at cloud base, which makes the cloud base
250 well pronounced. The difference between droplet concentrations in ST and NA experiments
251 decreases with height. The highest droplet concentration is reached in simulations where the CCN
252 activation spectrum was characterized by the slope parameter $k=0.5$. This can be attributed to the
253 fact that at $k=0.5$ the aerosol spectrum contains more CCN which are activated at cloud base than
254 at $k=0.9$.

255 Vertical profiles of the maximum values of droplet concentration and of cloud water content
256 (CWC) averaged over time periods of storm development (a-b) and over the mature stage (c,d) are
257 presented in **Figure 4**.

258 In NA the N_d maximum is reached near cloud base and the droplet concentration decreases
259 with height.. This behavior of $N_d(z)$ is more realistic than in ST, where N_d increases with height
260 up to an altitudes 2- 4 km, depending on the stage of storm evolution. This increase in the N_d in
261 ST is caused by in-cloud activation of mid-size CCN which were not activated at cloud base in the
262 standard approach. In NA, these CCN were activated at cloud base. There is, therefore, a negative
263 feedback in the supersaturation-droplet concentration relationship: an underestimation of
264 supersaturation at low levels in the ST simulations leads to the underestimation of droplet
265 concentration and to the corresponding increase in supersaturation at comparatively small
266 distances above cloud base. These results indicate that in models where droplet nucleation is
267 calculated only at cloud base, the correct calculation of S_{\max} at cloud base is *strictly necessary to*
268 *obtain reasonable values of N_d in clouds.*

269 At height of about 4-5 kms, droplet concentrations in ST and NA become nearly similar.
270 Figs. 4a,c show also that N_d is very sensitive to the slope parameter of the CCN activation
271 spectrum. The maximum N_d reached at cloud base is about 1100 cm^{-3} in EN3500-S-05 ($k=0.5$)
272 as compared to $\sim 550 \text{ cm}^{-3}$ in EN3500-S ($k=0.9$). This difference is caused by the fact that in case
273 $k=0.5$ the concentration of CCN with sizes exceeding $\sim 0.015 \mu\text{m}$ (which are activated at cloud
274 base) is larger than in case $k=0.9$ (see Fig.1).

275 The effect of the *smallest* CCN on N_d (and on entire ice microphysical structure) becomes
276 very important above 6 km. In simulations containing the smallest CCN, these CCN are activated
277 producing new small droplets at heights of around 6.5- 8 km. The increase in N_d is shown in Fig.
278 4a,c by red arrows. These smallest CCN are not activated at cloud base even in NA (where S_{\max}
279 is larger than S_w in ST). This in-cloud nucleation is caused by an increase in supersaturation at

280 these levels due to a decrease in CWC (Fig. 4b,d) and an increase in vertical velocity (not shown).
281 The increase in N_d by activation at high levels and its effect on concentration of ice crystals in
282 cloud anvils of deep convective clouds was also reported by Khain et al. (2012).

283 Since the slope parameter determines concentration both of larger CCN and of smallest
284 CCN, the slope parameter also affects the concentration of droplets nucleated at high levels.

285 Vertical profiles of CWC (Figs. 4b,d) are typical of deep convective clouds developing in
286 the highly polluted environment: CWC is large and has maximum at about 5 km, i.e. at quite high
287 altitude.

288 **Figure 5a** shows the vertical profiles of maximum concentration of plate crystals (in HUCM
289 homogeneous freezing leads to formation of plates) averaged over the mature stage of cloud
290 evolution (from 4860 to 5460s). The number concentration of ice crystals in E3500 and EN3500
291 (in which there are no the smallest CCN in the initial CCN spectrum) is by factor of 5 lower than
292 in simulations with the CCN spectra containing the smallest CCN. The results show that ice
293 crystal concentration in NA is higher only slightly than in ST. Thus *the concentration of ice*
294 *crystals in cloud anvils is determined to a large extent by the concentration of smallest CCN in*
295 *the CCN spectra and is substantially less sensitive to larger CCN, which are activated at cloud*
296 *base*. Figure 5b shows that this conclusion is valid for the entire period of the simulation. In
297 agreement with Fig. 4c, the concentration of plates increased when NA was used (**Fig. 5b**). The
298 comparative contribution of the smallest CCN and CCN additionally activated at the cloud base in
299 NA (as compared to ST) are shown in Fig. 5b by arrows.

300 **Figure 6** shows the vertical profiles of time averaged maximum mass contents of ice
301 crystals, snow, graupel and hail+freezing drops at the storm mature stage. The maximum

302 difference between ice crystal mass contents takes place at ~10-11 km, where ice crystals are
303 caused by homogeneous freezing.

304 The most pronounced effect of NA is an increase in the accretion rate. In agreement with
305 results of simulations of aerosol effects on ice microstructure of deep convective clouds (Khain
306 2009; Tao et al. 2012; Khain et al. 2016), the intensification of riming leads to a decrease in the
307 snow mass content and to an increase in the mass contents of graupel (Fig.6b-c).. The existence of
308 the smallest CCN concentration leads to further decrease in the snow mass content and to the
309 increase in the graupel mass content. This smallest CCN lead to higher supercooled droplet
310 concentration and to an increase in the liquid mass available for riming (Fig. 4d,e).

311

312 4.3. Low CCN concentration

313 In this section we compare the results for three pairs of simulations: a) E100 and EN100, b)
314 E100-S and EN100-S, and c) E100-S-0.5 and EN100-S-0.5 in which clouds were developed in the
315 atmosphere with low CCN concentration. After the first 35 min of cloud evolution, the cloud base
316 is located at 700-800 m altitude and $T=16.8^{\circ}\text{C}$ at this level.

317

318 The fields of droplet concentration N_d in different simulations at the developing stage of the
319 cloud evolution are shown in **Figure 7**. The maximum N_d in a NA is reached at cloud base, which
320 makes the cloud base well pronounced. The difference in droplet concentrations between ST and
321 NA simulations decreases with height. Although the difference is N_d between NA and ST is very
322 pronounced, the absolute difference is not large (about 20 cm^{-3}). This low N_d determines a
323 typical maritime microphysical structure of clouds in both NA and ST cases.

324 **Figure 8** shows vertical profiles of the maximum values of droplet concentration and cloud
325 water content (CWC) averaged over the time period of 3420-4020s (mature stage). One can see a
326 dramatic difference in the profiles of droplet concentration and between CWC values of at low
327 CCN concentration as compared to high CCN concentration (Fig. 4). At low CCN concentration,
328 droplet collisions are efficient and droplet concentration decreases with height much faster than in
329 polluted air. As a result, the CWC maximum at low CCN concentration is located at the height of
330 2 km as compared to 5 km in case of high CCN concentration. These differences determine the
331 huge difference in the ice microphysics.

332 Fig. 8 shows that both the droplet concentration and CWC are larger in NA as compared to
333 ST. The main differences between droplet concentrations near cloud base are, however,
334 determined by the difference in the slope parameter value: at $k=0.5$ there are more CCN of sizes
335 exceeding $0.015 \mu m$ than at $k=0.9$ (Fig. 1). These CCN are activated at cloud base leading to
336 higher concentration in simulations with $k=0.5$, especially when NA was applied.

337 Efficient collisions (seen by the sharp decrease in the CWC above $z=2$ km) and rain fall
338 decrease the droplet concentration. As a result, the supersaturation increases and leads to in-cloud
339 nucleation and an increase in the droplet concentration already at distances of a few hundred
340 meters above the cloud base. However, since the concentration of CCN is low, the amount of
341 new nucleated droplets in the simulations was only about $5-10 \text{ cm}^{-3}$. The second layer of intense
342 in-cloud nucleation caused by activation of the smallest CCN is seen within the altitude layer from
343 4 km to 8 km. The difference in droplet concentration within this layer is fully related to the
344 existence/absence of smallest CCN in the CCN size spectrum. The differences between droplet
345 concentration in ST and NA simulations are not significant at these levels.

346 This result agrees with the case of high CCN concentration when droplet concentration at
347 higher levels is to a large extent determined by the smallest CCN in the droplet spectrum.

348 **Figure 9** presents the vertical profiles of maximum mass contents of ice crystals, snow,
349 graupel and hail + freezing drops at the mature stage of cloud evolution. Comparison with Fig. 6
350 shows that with the exception of snow, the mass contents of different ice hydrometeors at low
351 CCN concentration are substantially lower than at high CCN concentration. The main reason for
352 such difference is lower CWC at low CCN concentration that leads to less intense riming and,
353 consequently to slow growth of ice particles.

354 Fig. 9 shows that the profiles of ice hydrometeors in NA and ST are similar. It means that
355 the ice microphysics is to a large extent determined by the mass of supercooled droplets at high
356 levels which in turn is determined by the *smallest* CCN in the CCN size spectrum. The effects of
357 the smallest CCN and the shape of CCN size spectra on droplet concentration and the
358 concentration on ice microphysics are much stronger than the effect of additional droplets
359 nucleating at cloud base in the NA. The reason for this effect was explained above.

360 The increase in the concentration of the smallest CCN and in droplet concentration leads to
361 an increase in the ice crystals mass content occurring about the level of homogeneous freezing
362 (Fig.9a).

363 The mass content of snow decreases with the increase in the smallest CCN concentration ,
364 because intensification of riming of snow leads to its conversion to graupel (Fig. 9b).
365 Consequently, the graupel mass content increases (Fig. 9c). As regards to mass content of hail,
366 the increase in the smallest CCN concentration leads to a decrease in the hail content above 6 km
367 and to its increase below this level (Fig. 9d). The higher hail mass content above 6 km layer in
368 the absence of smallest CCN is likely related to the fact the low droplet concentration leads to

369 formation of raindrops in high concentration. Although these raindrops are of comparatively small
370 size, the total raindrop mass content is larger than that in case of higher drop concentration. These
371 raindrops rapidly freeze above the freezing level producing hail (actually frozen drops) with total
372 mass larger than at high CCN concentration. This effect is discussed by Iltovich et al. (2016) in
373 detail. In HUCM, frozen raindrops are assigned to the hail category due to their high density. If
374 hail is defined as particles with sizes exceeding 1 cm, the amount of hail at low CCN
375 concentration would be negligible.

376

377 Higher hail mass content below 6 km in the presence of the smallest CCN can be attributed
378 to intense conversion of heavy rimed graupel to hail, as well as to more efficient hail growth by
379 riming. Note that sizes of hail particles forming in a deep convective cloud developing in the
380 polluted atmosphere are larger than hail forming in a cloud developing in clean air (Iltovich et al.
381 2016). Due to larger size, hail in the polluted case falls to the surface (Fig. 6d), while in clean air
382 hail melts at 1.5 km in the absence of small CCN, and in vicinity of the surface if the CCN size
383 spectrum contains the smallest CCN.

384 4.3 The impact on precipitation

385 **Figure 10a** shows the accumulated rain at surface in the polluted air. Accumulated rain
386 is maximum in EN3500-S-0.5 where effect of smallest CCNs is combined with the effect of
387 comparatively large amount of large CCN. This synergetic effect of the smallest and large CCN
388 is described by Khain et al. (2011). In most simulations, the masses of accumulated rain are
389 quite similar.

390 Comparison of Fig. 10a and Fig. 10 b shows that the accumulated rain at low aerosol
391 concentration is lower than at high CCN concentration, which is in agreement with many

392 previous studies. Accumulated rain in NA was found to be quite close to that in ST. The main
393 difference in the values of accumulated rain at low CCN concentration is caused by effects of
394 smallest aerosols increasing the mass of precipitating ice particles .

395 Amount of hail at the surface in polluted air (**Figure 10c**) is substantially larger than in
396 clean air (**Figure 10d**) due to lower sizes and faster melting of hail particles if CCN
397 concentration is low. The effect of AP on the size and amount of hail at the surface was
398 investigated by Ilotovitch et al. (2016) in detail.

399 Amount of hail at the surface in polluted air is slightly higher in EN3500-S-0.5 as
400 compared to E3500-S-0.5 (**Figure 10c**). We attribute this effect to a higher rate of riming in
401 EN3500-S-0.5 due to a higher amount of supercooled water (Fig. 4b, d). There are no
402 significant differences in the other cases of polluted air.

403 The main factor determining the differences in the amount of hail falling to the surface at
404 low CCN concentration is the effect of smallest CCN. The increase in concentration of smallest
405 CCN leads to an increase in hail growth by riming.

406 As regards to the ratio of hail amounts in the experiments with smallest AP, earlier or later
407 intensification of convective cells (which is more or less random) may affect the ratio. Since
408 the mass of hail falling to the surface in clean air is very low, a larger computational area is
409 required to obtain reliable statistics.

410

411 5. Conclusions

412 Sensitivity of the microphysics of deep convective clouds to the concentration of aerosols and
413 to the shape of aerosol size distribution is investigated using a new version of a 2D Spectral (bin)
414 Microphysics Cloud Model (HUCM). A new component of the model is the calculation of

415 maximum supersaturation at cloud base using the analytical expression derived by Pinsky et al.
416 (2012). The cloud microphysical structure obtained using this expression is compared with that
417 obtained with supersaturation calculated at model grid points.

418 The goal of the study was twofold: a) to test the effects of the improved calculation of
419 supersaturation maximum near cloud base (NA (new approach) vs ST (standard approach)) at
420 different aerosol loadings and b) to evaluate sensitivity of cloud microphysics to concentration and
421 shape of size distribution of aerosol particles. In the simulations, shape of CCN size distributions
422 was changed by changing the value of the slope parameter in the expression for activation
423 spectrum (the values of $k=0.5$ and $k=0.8$ were used) and by adding the smallest CCN with radii
424 below $0.015 \mu m$.

425 The values of S_{max} near cloud base calculated by the theoretical analysis were found to be
426 substantially larger than the supersaturation values calculated explicitly at model grid points
427 associated with cloud base. The comparison of the values of supersaturation at cloud base and
428 droplet concentration in the model simulations with the corresponding values calculated using a
429 benchmark parcel model showed that NA simulates cloud base supersaturation and droplet
430 concentration much more accurately than ST. Thus, *the first main conclusion* of the study is that
431 the droplet concentration field in NA is substantially more realistic than in ST, with the maximum
432 of droplet concentration in NA located near cloud base in agreement with classical results (Rogers
433 and Yau, 1989). The increased droplet concentration makes the cloud base more pronounced. The
434 improvement of the representation of the vertical profile of the droplet concentration is especially
435 significant in case of high CCN concentration, where utilization of S_{max} leads to a substantial
436 increase in the concentration of droplets near cloud base. Thus, even at 100-m vertical resolution,

437 it is necessary to use analytical expressions for S_{\max} . At low CCN concentration, the improved
438 representation of droplet concentration above cloud base has a comparatively weak effect on cloud
439 microphysics. This result can be attributed to the fact that droplet concentration increases
440 relatively slightly if it is more accurately calculated since the available CCN concentration is low.
441 As a result, intense warm rain rapidly arises in both NA and ST.

442 The error in calculation of droplet concentration near cloud base in ST is compensated to a
443 significant extent by in-cloud nucleation above cloud base. Indeed, in NA droplet concentration
444 increases with height up to level of 4 km (Fig. 4a). The only reason of such increase is the in-cloud
445 nucleation of comparatively large CCN.

446 Models with microphysical schemes that do not describe in-cloud droplet nucleation should
447 include calculation of S_{\max} at cloud base to avoid large errors in simulation of the microphysical
448 cloud structure.

449 *The second main conclusion* is high importance of the shape of CCN size distribution. Cloud
450 microphysics was found to be highly sensitive to the slope parameter of the CCN activation
451 spectra. The effect is comparable with the change in the total CCN concentration via the change
452 in the intercept parameter N_0 . The utilization of $k=0.5$ instead of $k=0.9$ nearly doubled droplet
453 concentration near cloud base that leads to corresponding effects on cloud microphysics, in
454 particular, to an increase in accumulated rain.

455 *The third main conclusion* is high sensitivity of ice microphysics to the existence of the
456 smallest CCN in the CCN size spectrum. Both in cases of low and high CCN concentration, the
457 differences in ice microphysics are determined to a large extent by *concentration of the smallest*
458 *aerosols in the CCN spectra*. In cases of high CCN concentration, the effect of the smallest CCN

459 in the NA becomes important above 5-6 km altitude where they are activated producing additional
460 supercooled liquid droplets. The latter leads to the increase in the concentration of ice crystals
461 above the level of homogeneous freezing by factor of about 5, to doubling of graupel mass
462 maximum. The smallest CCN also influence hail size and mass content.

463 In case of low CCN concentration the smallest CCN also lead to an increase in the
464 concentration and mass contents of ice crystals and to a significant increase of graupel and hail
465 mass contents. Note that many probes of CCN measure concentration of CCN at supersaturations
466 not exceeding 0.6%. In this case the concentration of the smallest CCN which remain non-
467 activated at this supersaturation remains unknown. Such measurements do not provide necessary
468 information for investigation of mixed-phase and ice microphysics.

469 Accumulated rain amount in case of high CCN concentration turned out to be higher than in
470 case of low CCN concentration. This result was discussed by Khain (2009) and Iltovich et
471 al.(2016) showing that formation of hail increases precipitation efficiency of mid-latitude storms.

472 Ice precipitation (calculated in mm of melted hail) at the surface is much lower than liquid
473 precipitation. Nevertheless, hail precipitation at the surface in case of high CCN concentration is
474 higher than in case of low CCN concentration by order of magnitude in agreement with results by
475 Khain et al. (2011) and Iltoviz et al. (2016). This effect can be attributed by formation of larger
476 hail particles in case of high CCN concentration (high supercooled mass content). The large hail
477 particles reach the surface, while smaller hail forming in case of low CCN concentration melts
478 without reaching the surface.

479 The concentrations of drops and ice crystals are important parameters determining cloud
480 radiative properties. In this context, more accurate calculation of the concentrations using the NA

481 as well as taking into account the effects of smallest CCN should improve the accuracy of
482 evaluation of radiative cloud properties. The proposed approach of calculation of nucleation of
483 droplets at cloud base is simple in the utilization and computationally efficient. It can be used in
484 cloud-resolved models with different vertical grid spacing. The utilization of cruder vertical model
485 resolution may lead to larger errors in cases when droplet concentration at cloud base is calculated
486 using supersaturations calculated at model grid points.

487 *Acknowledgements*

488 The study is supported by the US Department of Energy Award DE_FOA-0000647 from the U.S.
489 Department of Energy Atmospheric System Research Program, by the Binational US-Israel
490 Science Foundation (grant 2010446), and by the Israel Science Foundation (grant 1393/14).

491

492 **Appendix. Derivation of an expression for the supersaturation maximum at cloud base**

493 Detailed description of the derivation of Eq. (1) is given in Pinsky et al. (2012). Below we present
494 only a short description. Assuming that near cloud base $S_w \ll 1$, the equation for supersaturation
495 can be written as:

496

$$497 \quad \frac{dS_w}{dt} = A_1 \frac{dz}{dt} - A_2 \frac{dq_w}{dt} \quad (A1)$$

498

499 where coefficients A_1 and A_2 are presented in **Table 1**; z is the height above cloud base and q_w
500 is liquid water mixing ratio. The first term on the right-hand side of eq. (A1) describes an
501 increase in supersaturation due to adiabatic air cooling during ascent, whereas the second term

502 describes the supersaturation decrease caused by condensation of water vapor on droplets.

503 Integration of equation (A1) leads to the equation of mass balance:

$$504 \quad S_w = A_1 z - A_2 q_w + C_1 \quad (A2)$$

505 where $C_1 = 0$ at cloud base. Assuming monodisperse DSD with droplets of radii r , the liquid

506 water mixing ratio can be written as :

$$507 \quad q_w = \frac{4}{3} \pi \frac{\rho_w}{\rho_a} N_d r^3 \quad (A3)$$

508 where N_d is the droplet concentration. The equation for diffusional growth can be written is the

509 form where the curvature term and the chemical term are omitted (Pinsky et al. 2012):

$$510 \quad \frac{dr}{dt} = \frac{1}{Fr} S_w \quad (A4)$$

511 The expression for coefficient F is presented in **Table 1**. Coefficients A_1 , A_2 and F slightly

512 depend on temperature and can be assumed constant in the analysis. Using Eqs. (A2-A4), eq. (1)

513 can be rewritten in the closed form as:

$$514 \quad \frac{dS_w}{dz} = A_1 - \frac{1}{w} B_1 (A_2 N_d)^{2/3} (A_1 z - S_w)^{1/3} S_w \quad (A5)$$

$$515 \quad \text{where } B_1 = \frac{3}{F} \left(\frac{4\pi \rho_w}{3 \rho_a} \right)^{2/3}$$

516 Pinsky et al. (2012) showed that Eq. (A5) can be written in a non-dimensional form that

517 results in an universal profile of supersaturation with height at given vertical velocity. The

518 condition $\frac{dS_w}{dz} = 0$ applied to this equation allows to get solution in the form (1) for S_{\max} , as

519 well as for the height of S_{\max} over the cloud base. Pinsky et al. (2012, 2014) showed that (1) is
520 valid for any size distributions of CCN.

521

522

523

524

525

526

527

528

529

530

531

532

533

534

535 **References**

536 Abdul-Razzak, H., and S. J. Ghan (2000), A parameterization of aerosol activation: 2.
537 Multiple aerosol types, *J. Geophys. Res.*, *105*(D5), 6837, doi:10.1029/1999JD901161.

538 Abdul-Razzak, H., S. J. Ghan, and C. Rivera-Carpio (1998), A parameterization of aerosol
539 activation: 1. Single aerosol type, *J. Geophys. Res.*, *103*(D6), 6123, doi:10.1029/97JD03735.

540 Benmoshe, N., M. Pinsky, A. Pokrovsky, and A. Khain, 2012: Turbulent effects on the
541 microphysics and initiation of warm rain in deep convective clouds: 2-D simulations by a
542 spectral mixed-phase microphysics cloud model. *J. Geophys. Res.*, **117**, D06220,
543 doi:10.1029/2011JD016603.

544 Bedos, C., K. Suhre, and R. Rosset (1996), Adaptation of a cloud activation scheme to a
545 spectral-chemical aerosol model, *Atmos. Res.*, *41*(3-4), 267–279, doi:10.1016/0169-
546 8095(96)00014-2.

547 Bigg, E. K., 1953: The formation of atmospheric ice crystals by the freezing of droplets.
548 *Quart. J. Roy. Meteor. Soc.*, *79*, 510–519, doi:10.1002/qj.49707934207.

549 Cohard, J.-M., J.-P. Pinty, and C. Bedos (1998), Extending Twomey's Analytical Estimate
550 of Nucleated Cloud Droplet Concentrations from CCN Spectra, *J. Atmos. Sci.*, *55*(22), 3348–
551 3357, doi:10.1175/1520-0469(1998)055<3348:ETSAEO>2.0.CO;2.

552 Fountoukis, C. (2005), Continued development of a cloud droplet formation
553 parameterization for global climate models, *J. Geophys. Res.*, *110*(D11), D11212,
554 doi:10.1029/2004JD005591.

555 Freud E., and D. Rosenfeld, 2012: Linear relation between convective cloud drop
556 number concentration and depth for rain initiation. *J. Geophys. Res.* **117**, D02207.

557 Ghan, S. J., C. C. Chung, and J. E. Penner (1993), A parameterization of cloud droplet
558 nucleation part I: single aerosol type, *Atmos. Res.*, *30*(4), 198–221, doi:10.1016/0169-
559 8095(93)90024-I.

560 Ghan, S. J., L. R. Leung, R. C. Easter, and H. Abdul-Razzak (1997), Prediction of cloud
561 droplet number in a general circulation model, *J. Geophys. Res.*, *102*(D18), 21777,
562 doi:10.1029/97JD01810.

563 Ghan, S. J., H. Abdul-Razzak, A. Nenes, Y. Ming, X. Liu, M. Ovchinnikov, B. Shipway,
564 N. Meskhidze, J. Xu, and X. Shi (2011), Droplet nucleation: Physically-based
565 parameterizations and comparative evaluation, *J. Adv. Model. Earth Syst.*, *3*(4), n/a–n/a,
566 doi:10.1029/2011MS000074.

567 Heymsfield A. J., A. Bansemer, G. Heymsfield and A.O. Fierro (2009), Microphysics of
568 maritime tropical convective updrafts at temperatures from -20 oC to -60 oC, *J. Atmos. Sci.*, *66*,
569 3530-3565.

570 Ilotoviz, E., A. Khain, N. Benmoshe, V. T. J. Phillips, and A. Ryzhkov, 2016: Effect of
571 aerosols on freezing drops, hail and precipitation in a mid-latitude storm. *J. Atmos. Sci.*, *73*,
572 109-144, <http://dx.doi.org/10.1175/JAS-D-14-0155.1>.

573 Khain, A. P., 2009: Notes on state-of-the-art investigations of aerosol effects on
574 precipitation: A critical review. *Environ.Res. Lett.*, *4*, 015004, doi:10.1088/1748-
575 9326/4/1/015004.

576 Khain, A., M. Ovtchinnikov, M. Pinsky, A. Pokrovsky, and H. Krugliak (2000), Notes on
577 the state-of-the-art numerical modeling of cloud microphysics, *Atmos. Res.*, **55**(3-4), 159–224,
578 doi:10.1016/S0169-8095(00)00064-8.

579 Khain, A. P., Benmoshe, N. and A. Pokrovsky, 2008: Factors Determining the Impact of
580 Aerosols on Surface Precipitation from Clouds: An Attempt at Classification, *J. Atmos. Sci.*,
581 **65**(6), 1721–1748, doi:10.1175/2007JAS2515.1.

582 Khain, A.P., D. Rosenfeld, A. Pokrovsky, U. Blahak, and A. Ryzhkov (2011), The role of
583 CCN in precipitation and hail in a mid-latitude storm as seen in simulations using a spectral
584 (bin) microphysics model in a 2D dynamic frame, *Atmos. Res.*, **99**(1), 129–146,
585 doi:10.1016/j.atmosres.2010.09.015.

586 Khain, A.P., V. Phillips, N. Benmoshe, and a. Pokrovsky, 2012: The Role of Small Soluble
587 Aerosols in the Microphysics of Deep Clean Clouds, *J. Atmos. Sci.*, **69**(9), 2787–2807,
588 doi:10.1175/2011JAS3649.1.

589 Khain A.and B. Lynn And J. Shpund, 2016: High Resolution WRF Simulations of
590 Hurricane Irene: Sensitivity to Aerosols and Choice of Microphysical schemes. *Atmos.*
591 *Research*. Volume 167, 1 January 2016, 129–145.

592 Khvorostyanov, V. I., and J. a. Curry (2006), Aerosol size spectra and CCN activity
593 spectra: Reconciling the lognormal, algebraic, and power laws, *J. Geophys. Res.*, **111**(D12),
594 D12202, doi:10.1029/2005JD006532.

595 Kogan Y.L. 1991: The simulation of a convective cloud in a 3-D model with explicit
596 microphysics. Part I: Model description and sensitivity experiments. *J. Atmos. Sci.*, **48**,
597 1160–1189.

598 Meyers, M. P., P. J. DeMott, and W. R. Cotton, 1992: New primary ice-nucleation
599 parameterizations in an explicit cloud model. *J. Appl. Meteor.*, **31**, 708–721.

600 Phillips, V. T. J., A. Pokrovsky, and A. Khain, 2007: The influence of time-dependent
601 melting on the dynamics and precipitation production in maritime and continental storm clouds.
602 *J. Atmos. Sci.*, **64**, 338–359, doi:10.1175/JAS3832.1.

603 Phillips, V. T. J., A. Khain, N. Benmoshe, A. Ryzhkov, and E. Ilotovich, 2014: Theory of
604 time dependent freezing. Part I: Description of scheme for wet growth of hail. *J. Atmos. Sci.*,
605 **71**, 4527–4557, doi:10.1175/JAS-D-13-0375.1.

606 Phillips, V. T. J., A. Khain, N. Benmoshe, A. Ryzhkov, and E. Ilotovich, 2015: Theory of
607 time dependent freezing. Part II: Scheme for freezing raindrops and simulations by a cloud
608 model with spectral bin microphysics. *J. Atmos. Sci.*, **72**, 262–286, doi:10.1175/JAS-D-13-
609 0376.1.

610 Pinsky, M., Khain, A. P.: 2002 Effects of in-cloud nucleation and turbulence on droplet spectrum
611 formation in cumulus clouds. *Quart. J. Roy. Met. Soc.*, 128, 1-33.

612 Pinsky M., I. Mazin, A. Korolev and A. Khain (2012), Analytical estimation of droplet
613 concentration at cloud base, *J. Geophys. Res.* **117**, D18211, 14 PP.

614 Pinsky M., I.P. Mazin, A. Korolev, and A. Khain, 2013: Supersaturation and diffusional
615 droplet growth in liquid clouds. *J. Atmos. Sci.* **70**, 2778-2793

616 Pinsky M., I. Mazin, A. Korolev and A. Khain (2014) Supersaturation and diffusional
617 droplet growth in liquid clouds: Polydisperse spectra . *J. Geophys Res.* 2014, 119, 12872-
618 12887.

619 Pruppacher, H.R., Klett, J.D., 1997. *Microphysics of Clouds and Precipitation*. 2nd edn.
620 Oxford Press, 914 p.

621 Rogers R. R. and Yau M. K, 1989: *A Short Course in Cloud Physics*, Pergamon press.
622 293pp.

623 Rosenfeld, D., U. Lohmann, G. B. Raga, C. D. O'Dowd, M. Kulmala, S. Fuzzi, A.
624 Reissell, and M. O. Andreae (2008), Flood or drought: how do aerosols affect precipitation?,
625 *Science*, 321(5894), 1309–13, doi:10.1126/science.1160606.

626 Rotunno, R., and J. Klemp (1985), On the Rotation and Propagation of Simulated
627 Supercell Thunderstorms, *J. Atmos. Sci.*, 42(3), 271–292, doi:10.1175/1520-
628 0469(1985)042<0271:OTRAPO>2.0.CO;2.

629 Segal Y. and Khain, A. P., 2006: Dependence of droplet concentration on aerosol
630 conditions in different cloud types: application to droplet concentration parameterization of
631 aerosol conditions, *J. Geophys. Res.* Vol. 111, D15204, doi:10.1029/2005JD006561

632 Shipway, B. J., and S. J. Abel (2010), Analytical estimation of cloud droplet nucleation
633 based on an underlying aerosol population, *Atmos. Res.*, 96(2-3), 344–355,
634 doi:10.1016/j.atmosres.2009.10.005.

635 Takahashi, T., Endoh, T., Wakahama, G., 1991. Vapor diffusional growth of free-falling snow
636 crystals between -3 and -23°C . *J. Meteorol. Soc. Jpn.* 69, 15–30.

637 Tao W.-K., Jen-Ping Chen, Zhanqing Li, Chien Wang, Chidong Zhang (2012), Impact of
638 Aerosols on Convective Clouds and Precipitation. *Reviews of Geophysics*. [50, Issue 2](#), June
639 2012 DOI: 10.1029/2011RG000369.

640 Vali, G., 1994: Freezing rate due to heterogeneous nucleation. *J. Atmos. Sci.*, 51, 1843–
641 1856, doi:10.1175/1520-0469(1994)051,1843:FRDTHN.2.0.CO;2.

642

643

644

645

646

647

648

649

650

651 **Table 1. List of symbols**

652

653

Symbol	Description	Units
A	$\frac{2\sigma_w}{\rho_w R_v T}$	m

A_1	$\frac{g}{R_a T} \left(\frac{L_w R_a}{c_p R_v T} - 1 \right)$	m^{-1}
A_2	$\frac{1}{q_v} + \frac{L_w^2}{c_p R_v T^2}$	-
B	$\frac{v_n \Phi_s \varepsilon_m M_w \rho_n}{M_n \rho_w}$	-
B_1	$\frac{3}{F} \left(\frac{4\pi\rho_w}{3\rho_a} \right)^{2/3}$	$\text{m}^2 \text{s}$
C_1	$1.058 (FA_1 / 3)^{3/4} \left(\frac{3\rho_a}{4\pi\rho_w A_2} \right)^{1/2}$	$\text{m}^{9/4} \text{s}^{-3/4}$
c_p	specific heat capacity of moist air at constant pressure	$\text{J kg}^{-1} \text{K}^{-1}$
D	coefficient of water vapor diffusion in the air	$\text{m}^2 \text{s}^{-1}$
e		
e_w	saturation vapor pressure above the flat surface of water	N m^{-2}
g	acceleration of gravity	m s^{-2}
F	$\left(\frac{\rho_w L_w^2}{k_a R_v T^2} + \frac{\rho_w R_v T}{e_w (T) D} \right)$	$\text{m}^{-2} \text{s}$
K	parameter of activity spectra	
k_a	coefficient of air heat conductivity	$\text{J m}^{-1} \text{s}^{-1} \text{K}^{-1}$
L_w	latent heat for liquid water	J kg^{-1}
M_n	molecular weight of aerosol salt	kg mol^{-1}
M_w	molecular weight of water	kg mol^{-1}
N_d	concentration of liquid droplets	m^{-3}
N_0	parameter of activation spectra	
P	pressure of moist air	N m^{-2}
q_v	water vapor mixing ratio (air)	kg kg^{-1}
q_w	liquid water mixing ratio	kg kg^{-1}
r_{\max}	drop radius at $z = z_{\max}$	m
		-
S_w	$S_w = e/e_w - 1$ supersaturation over water	-

S_{\max}	supersaturation maximum	-
T	absolute temperature	$^{\circ}\text{K}$
T_{C}	temperature at cloud base	$^{\circ}\text{C}$
w	vertical velocity	m s^{-1}
z	height over condensation level	m
z_{\max}	height of supersaturation maximum	m
ε_m	soluble fraction	-
ρ_a	density of air	kg m^{-3}
ρ_N	density of a dry aerosol particle	kg m^{-3}
ρ_w	density of liquid water	kg m^{-3}
σ_w	surface tension of water-air interface	Nm^{-1}
v_n	van 't Hoff factor	-

654

655

656

657

658

659

660

661 **Table 2.** CCN concentrations in different experiments in the boundary layer

	High CCN concentration, cm^{-3}		Low CCN concentration, cm^{-3}	
Slope	No smallest CCN	With smallest CCN	No smallest CCN	With smallest CCN

parameter				
k=0.9	840	2930	33	214
k=0.5	1552	3140	53	152

662

663

664

665

666

667

668

669

670

671

672

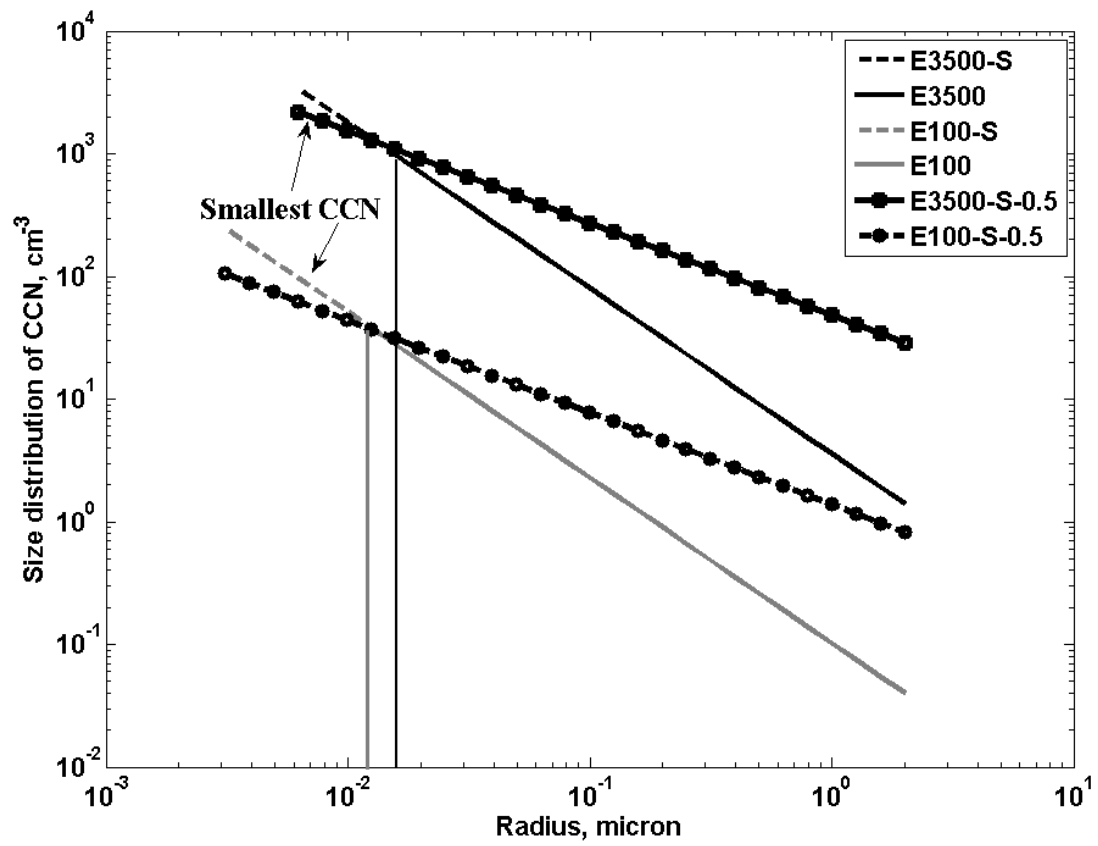
673

674

675

676 **Figures**

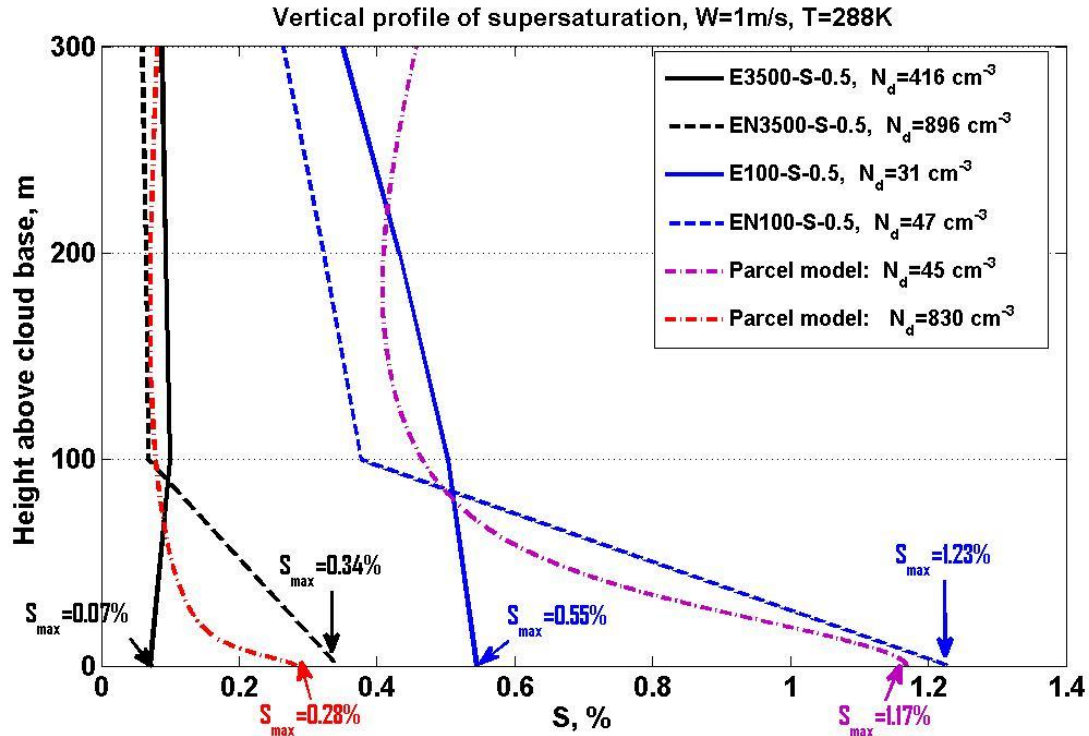
677



678

679 **Figure 1.** The initial size distributions of aerosols near the surface in different simulations.

680



681

682 **Figure 2.** Examples of vertical profiles of the supersaturation above cloud base calculated using
 683 HUCM and a benchmark parcel model. The columns with w close to 1 m/s at cloud base were
 684 chosen for comparison. The values of S_{max} in HUCM were calculated according to *Pinsky et al.*
 685 (2012). The values of droplets concentration calculated at cloud base in different simulations
 686 are shown as well (see legend box).

687

688

689

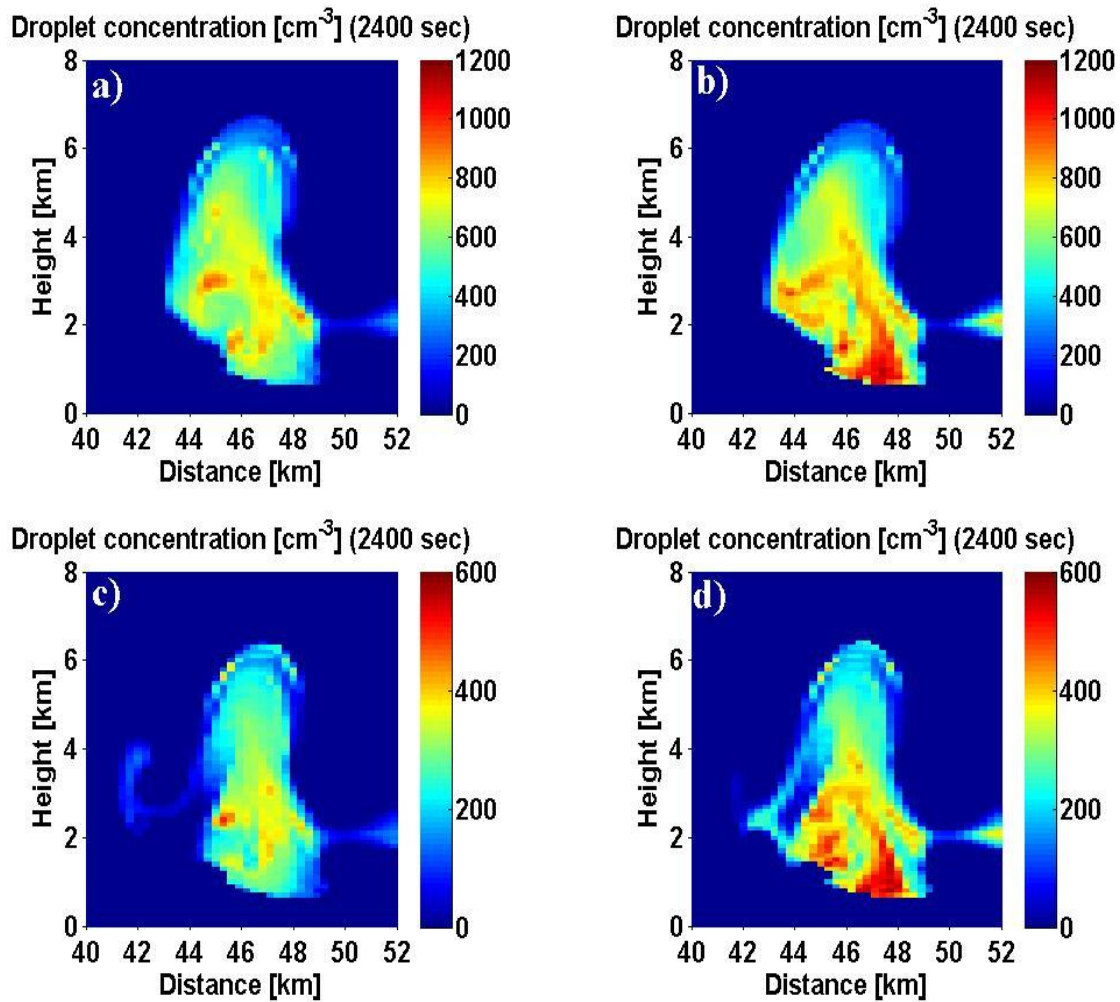
690

691

692

693

694



696

697

698

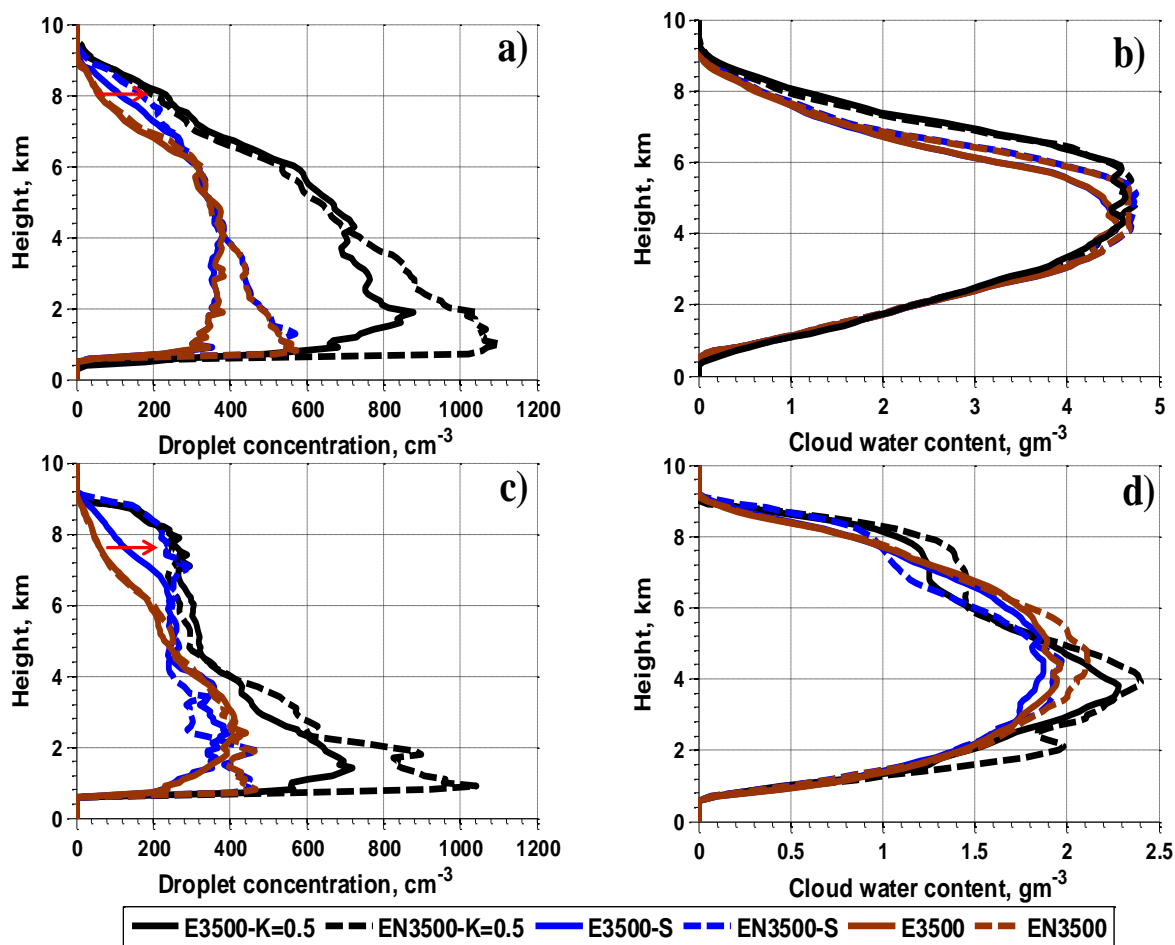
699 **Figure 3.** Field of droplet concentration at $t=2400$ s in (a) E3500-S-0.5, (b) EN3500-S-0.5, (c)
 700 E3500-S and (d) EN3500-S.

701

702

703

704



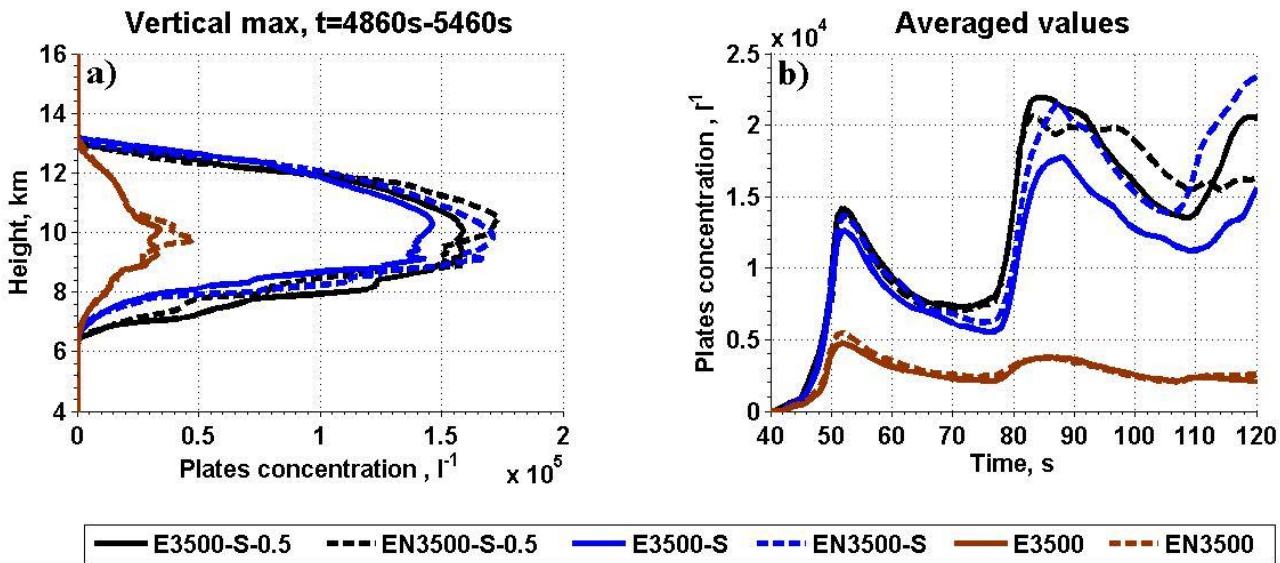
706

707

708 **Figure 4.** Vertical profiles of the maximum values of droplet concentration (a,d) and CWC(b,e)
 709 in simulations with high CCN concentration. The profiles are obtained by averaging over the
 710 time period of 2400-3000s (upper row) and over time period of 4860-5460s (bottom row). Panel
 711 (c) shows a zoom of panel (b) for large CWC .

712

713



714

715

716

717

718 **Figure 5.** Vertical profiles of (a) maximum values of plates concentration and (b) time
 719 dependencies of averaged plate concentration. The profiles are obtained by averaging over the
 720 time period of 4860-5460s. The low and the upper arrows in the panel b show approximate
 721 contribution of smallest CCN and the additional CCN activated in NA, respectively.

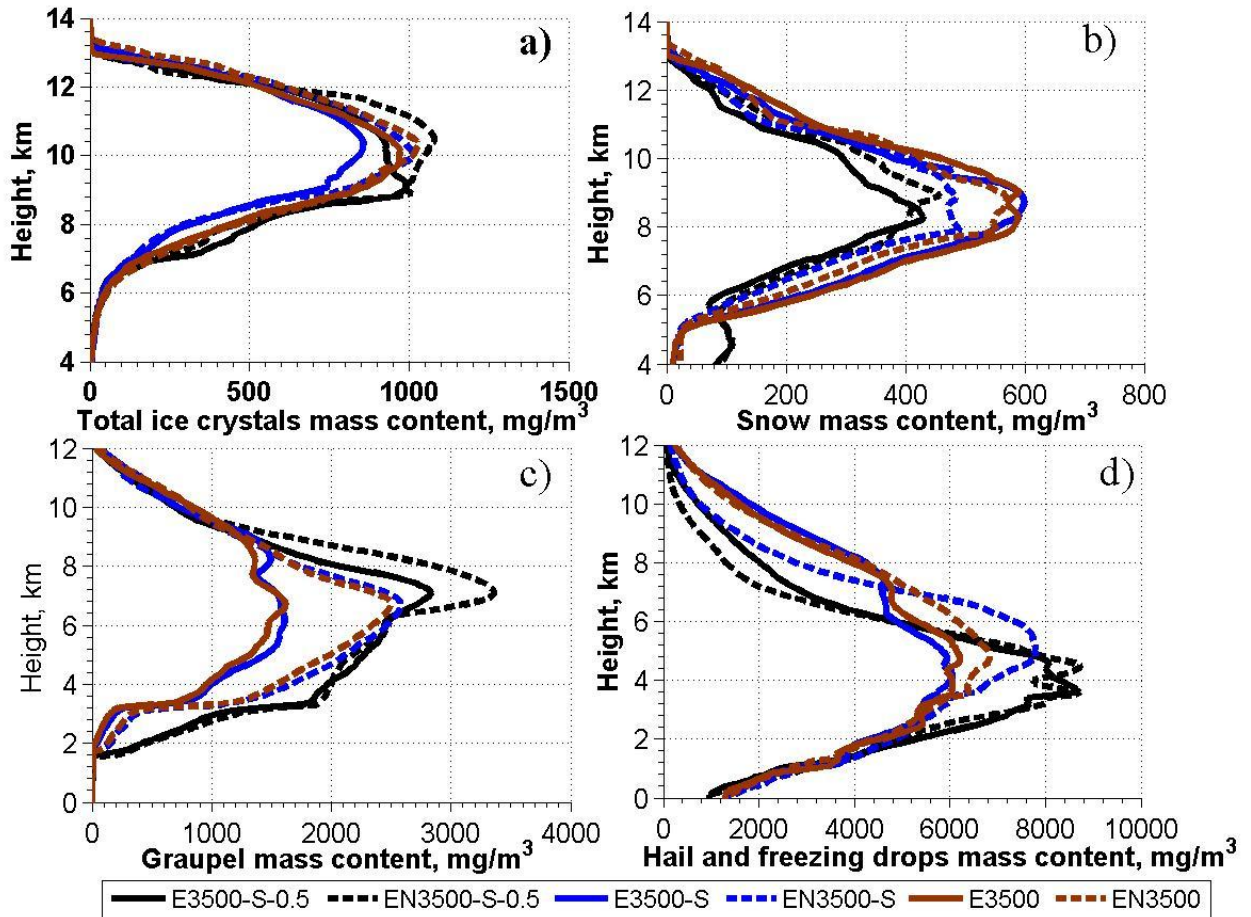
722

723

724

725

726



727

728

729 **Figure 6.** Vertical profiles of the maximum values of mass content: (a) total ice crystals, (b)
 730 snow, (c) graupel and (d) total hail and freezing drops in simulations with high CCN
 731 concentration. The profiles are obtained by averaging over the time period of 4860-5460s.

732

733

734

735

736

737

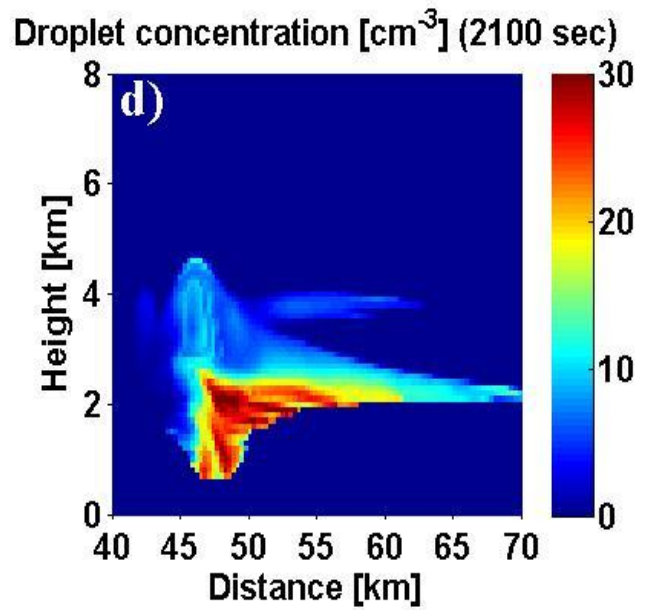
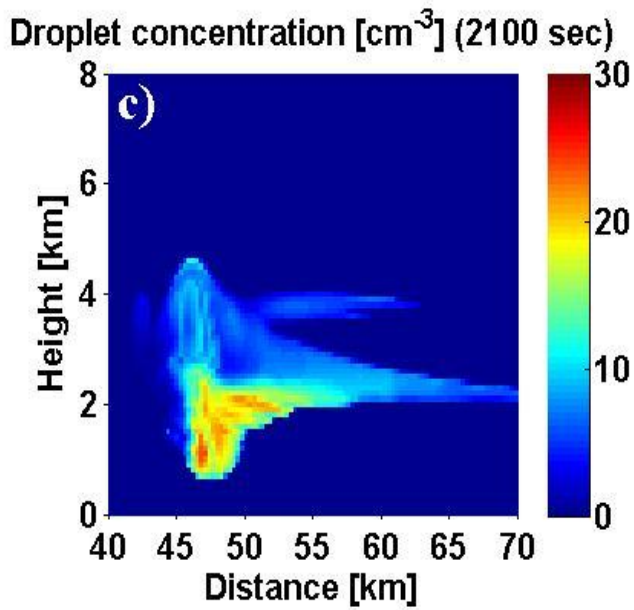
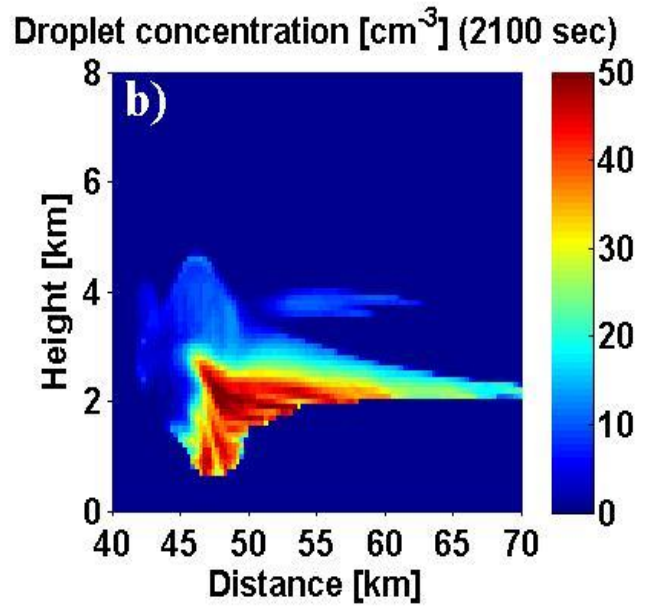
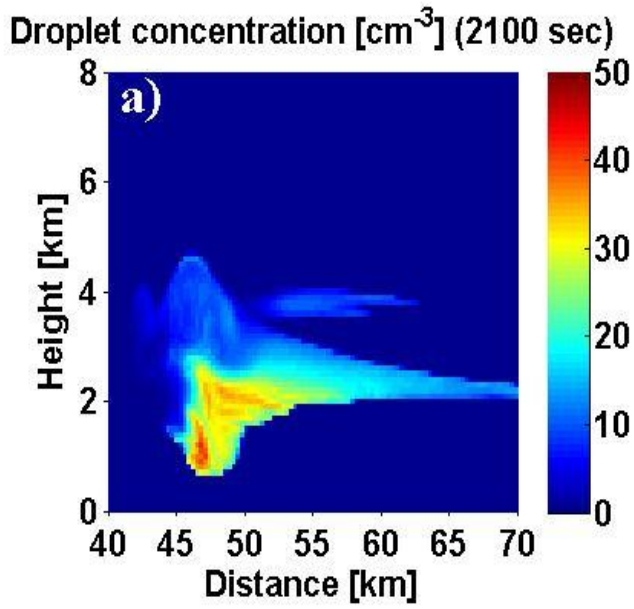
738

739

740

741

742



743

744

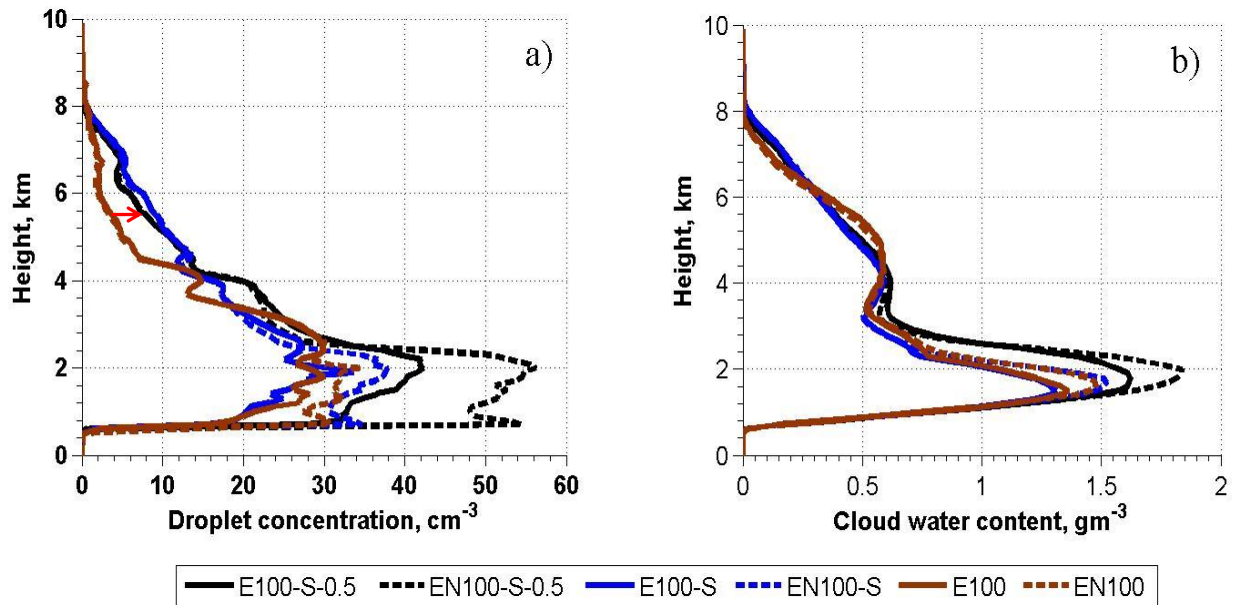
745

746 **Figure 7.** Field of droplet concentration at $t=2100s$ in (a) E100-S-0.5, (b) EN100-S-0.5, (c)
 747 E100-S and (d) EN100-S simulations.

748

749

750
751
752

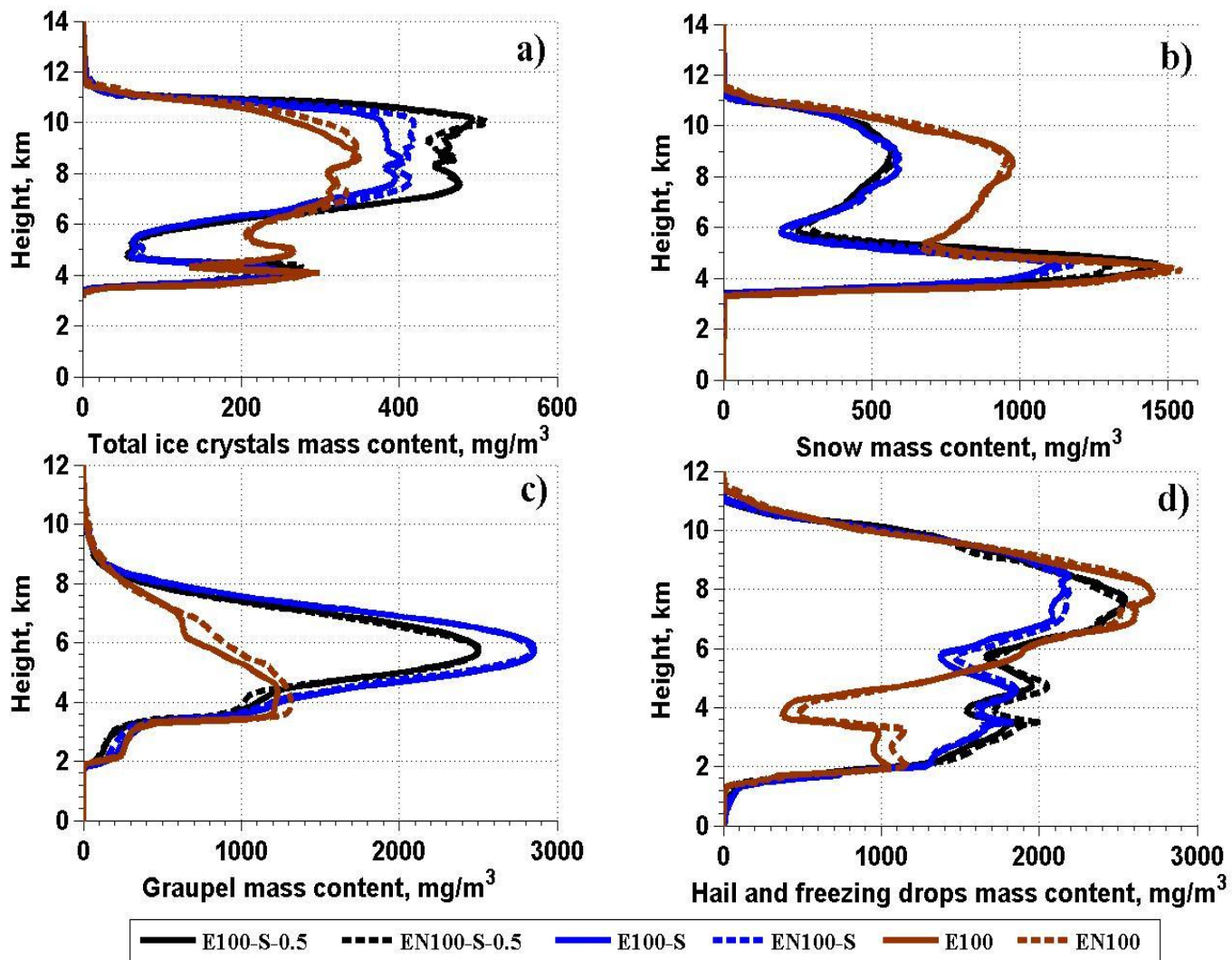


753

754

755 **Figure 8.** Vertical profiles of the maximum values of droplet concentration (a) and CWC (b) in
756 simulations with low CCN concentration ($N_0 = 100 cm^{-3}$). The profiles are obtained by
757 averaging over the time period of 3420-4020s. Red arrow shows the increase in droplet
758 concentration due to in-cloud nucleation in simulations with the CCN spectra containing small
759 CCN.

760
761
762
763



764

765

766 **Figure 9.** Vertical profiles of the maximum values of mass content: (a) total ice crystals, (b)
 767 snow, (c) graupel and (d) total hail and freezing drops in the simulations with low CCN
 768 concentration. The profiles are obtained by averaging over the time period of 3420-4020s.

769

770

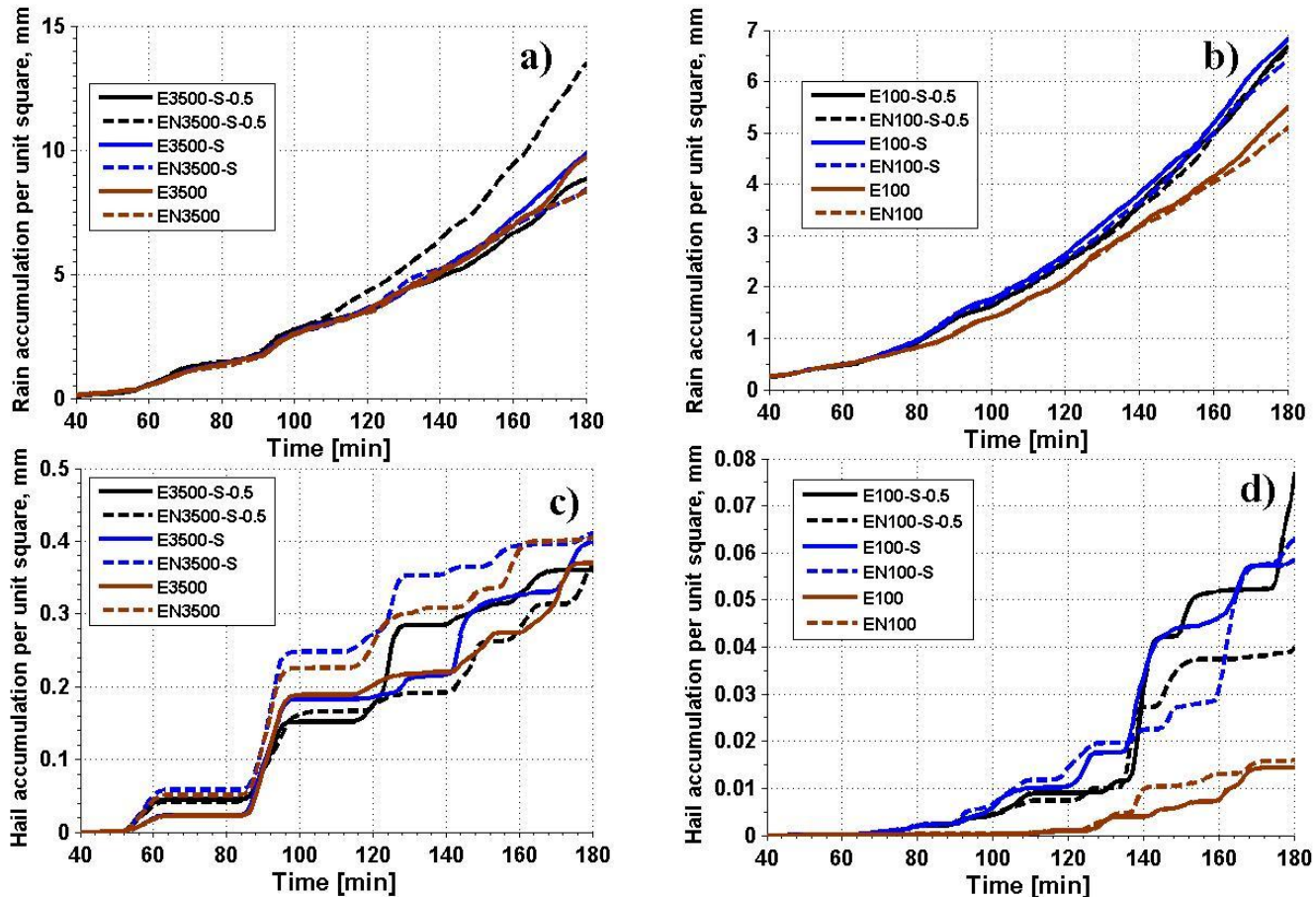
771

772

773

774

775



776

777

778

779 **Figure 10.** Time dependencies of (a) accumulated rain at surface for polluted and (b) for clean.
780 Accumulated hail at the surface for polluted (c) and for clean (d) in different simulations in
781 polluted cases.